Monthly Notices
of the
ROYAL ASTRONOMICAL SOCIETY

Mon. Not. R. Astron. Soc. **419,** 3521–3528 (2012) doi:10.1111/j.1365-2966.2011.19990.x

Variation of the area-to-mass ratio of high area-to-mass ratio space debris objects

C. Früh⋆ and T. Schildknecht⋆

Astronomical Institute, University of Bern, Sidlerstrasse 5, 3012 Bern, Switzerland

Accepted 2011 October 12. Received 2011 October 11; in original form 2011 August 10

ABSTRACT

An unexpected space debris population with the unique property of a very high area-to-mass ratio (HAMR) was detected in 2004 by Schildknecht and colleagues. Ever since, attempts have been made to investigate the dynamical properties of these objects further. Their orbits are heavily perturbed by the effect of direct radiation pressure, and unknown attitude motion complicates orbit prediction. The area-to-mass ratio of the objects seems to be unstable over time. Only sparse optical data are available for these objects in drift orbits.

This paper makes use of optical observations of five HAMR objects, observed over several years, and investigates the variation of their area-to-mass ratio and orbital parameters. A normalized orbit determination setup is established and validated with two low- and two high-area-to-mass-ratio-objects, to ensure that comparable orbits over longer time spans are determined even with sparse optical data.

Key words: methods: data analysis – Catalogues – celestial mechanics – ephemeredes – minor planets, asteroids: individual: space debris.

1 INTRODUCTION

The Astronomical Institute of the University of Bern (AIUB) detected high area-to-mass ratio (HAMR) objects in GEO-like orbits in 2004 (Schildknecht et al. 2003, 2004, 2005a). Since then, the AIUB has observed HAMR objects on a regular basis and keeps a small catalogue of HAMR and other space debris objects that are not listed in the USSTRATCOM catalogue. The observations are performed with the 1-m ESA Space Debris Telescope (ESASDT), located on Tenerife, Spain, and with the 1-m Zimmerwald Laser and Astrometry Telescope (ZIMLAT), located in Zimmerwald, Switzerland. Additional observations for some objects, which were detected by the AIUB, are provided courtesy of the Keldysh Institute of Applied Mathematics, Moscow, via the ISON network.

Maintaining a catalogue of HAMR objects is especially challenging because of the unique properties of these objects: the orbits are highly perturbed by direct radiation pressure. Regular observations on short time intervals are mandatory. Variations in the value of the effective area-to-mass ratio (AMR) were detected in routine orbit determinations for catalogue maintenance, and preliminary investigations were then performed (Musci et al. 2010).

For the investigations presented in this paper, orbits were determined with an enhanced version of the CelMech tool (Beutler 2005). The AMR value is determined as a scaling parameter of the direct radiation pressure. The acceleration resulting from the direct radiation pressure is calculated as

$$\boldsymbol{a}_{\mathrm{rad}} = \frac{C}{2}\,\frac{S}{c}\,\frac{AU^2}{|\boldsymbol{r}-\boldsymbol{r}_{\odot}|^2}\,\frac{A}{m}\,\frac{\boldsymbol{r}-\boldsymbol{r}_{\odot}}{|\boldsymbol{r}-\boldsymbol{r}_{\odot}|}, \tag{1}$$

where $\boldsymbol{r}$ is the geocentric position of the satellite, $\boldsymbol{r}_{\odot}$ is the geocentric position vector of the Sun, AU is the astronomical unit, A is the effective cross-section exposed to radiation, m is the mass of the satellite, and c is the speed of light. C is the reflection coefficient. The direct radiation pressure is determined under the assumption of a spherically shaped object. In contrast to the calculation of the radiation pressure acceleration by other sources (see, for example, Vallado & McCain 2001), the coefficient C is divided by two in the formula above. A value for C has to be chosen: by default, 2.0 is selected in the standard processing. This corresponds to an assumption of full absorption. All AMR values presented in this paper have to be interpreted as the effective AMR scaled by $C/2 = 1$; the AMR values of other sources may be scaled by a different factor. It is assumed that the AMR is constant over the orbital fit interval. A default value of $0.02\,\mathrm{m^2\,kg^{-1}}$ is selected, which corresponds to an AMR value of a standard GPS satellite; in this case the AMR parameter is not estimated but is kept fixed in the orbit determination. For HAMR objects an AMR value is always estimated.

The shadow paths of the orbit are modelled under the assumption of a spherical earth on a mean circular orbit, the boundary between sunlit and eclipsed parts is assumed to be cylindrical, no distinction between penumbra and umbra is made, and the earth's atmosphere is neglected.

⋆E-mail: frueh@aiub.unibe.ch (CF); thomas.schildknecht@aiub.unibe.ch (TS)

Table 1. Internal name, eccentricity, inclination (°), semimajor axis (km), area-to-mass ratio ($m^2\,kg^{-1}$) and apparent magnitude (mag) of selected objects of the AIUB catalogue.

Name	Epoch	*a*	*e*	*i*	AMR	Mag
E03174A	55208.0	41900	0.001	10.1	0.01	14.6
E06321D	55275.9	41400	0.035	7.00	2.29	15.3
E06327E	54470.1	40000	0.067	12.31	0.20	17.2
E08241A	55213.0	41600	0.041	13.26	1.24	16.1

For a long-term investigation of the orbits and the AMR values, different comparable orbits have to be determined. Only sparse observations are available, which are unequally spaced in time. A normalized setup is developed, tested with two low-AMR objects and two of the HAMR objects in the AIUB catalogue, and applied for the creation of comparable orbits for the investigation of the HAMR objects.

2 NORMALIZED SPARSE DATA SETUP

2.1 Method

Four representative GEO objects from the internal catalogue of the AIUB were chosen: they have been followed over longer time periods and are not listed in the USSTRATCOM catalogue. These objects are clearly space debris, as no manoeuvres could be detected in the data. The AIUB did not have information on what these objects actually were before becoming debris. From the apparent magnitude it can be concluded that they are all fragmentation pieces. They represent typical objects found in GEO surveys. Their properties are listed in Table 1.

Two of the objects have low AMRs, and two objects qualify as HAMR objects, with an AMR value larger than 1 $m^2\,kg^{-1}$. The optical angle-only observations were obtained with ZIMLAT (Zimmerwald, Switzerland) and ESASDT (Tenerife, Spain), supplemented by some observations from the ISON network provided by the Keldysh Institute of Applied Mathematics, Moscow, Russia. The latter observations were obtained from various sites of the ISON network – in these particular cases, all located in Eastern Europe.

All orbits were determined from two observation sets only, using a priori orbital elements. A maximum of eight observations are allowed per set. An observation set may consist of more than one tracklet. However, the observations within the sets should not be distributed over more than three days.

Orbits were determined for different spacings of two observation sets stemming (i) from one observation site only and (ii) from multiple sites. In the first case, the observations stem either from ZIMLAT or from ESASDT only. In the second case, not only were the observations of ZIMLAT and ESASDT combined, but also observations from the ISON network were used, if available. When observations from different sites are used in orbit determination, the distribution is either that the first set of observations stems from one site and the second from another, or that there are observations from different sites at similar epochs used within the first and/or the last set of observations, or a mixture of those options. In the figures, the label *ALL* is applied when observations of ZIMLAT (labelled *ZIM*), the ESASDT and of the ISON network are combined; the label *SDT-ZIM* is applied if only the observations of ZIMLAT and the ESASDT are used. The distances between the observations and the ephemerides of the predicted orbits of the four objects for a prediction interval of 50 d after the last observation used for orbit determination were determined. The distances were averaged and a mean value and standard deviation were calculated. Between six and 50 single distances between ephemerides and observations were averaged.

The predicted ephemeris positions were compared with the optical angle-only observations, which were not used in orbit determination. Angular distances were determined on the celestial sphere. The observations used for the comparison stem from ZIMLAT and ESASDT and serve as ground truth. Calibration measurements with high accuracy ephemerides of Global Navigation Satellite System (GNSS) satellites provided by the International GNSS Service (IGS) showed an accuracy of the measurements of ZIMLAT and ESASDT of below 1 arcsec. Validation that the further observations do in fact belong to the same object was obtained via an orbit determination with both the observations used in the original sparse data orbit determination and the observations that they were compared with. An orbit determination with a root-mean-square of below 2 arcsec is a reliable tool with which to associate observations of this accuracy of the same object with each other, as shown with cluster observations in Musci et al. (2005).

2.2 Results

In Fig. 1 the angular distance between predicted and observed positions is displayed as a function of the time interval between the first and the last observations that were used in orbit determination. Displayed are the mean values and the standard deviations of the angular distances of the single orbits. The mean value and standard deviations are determined with all single angular distances of predicted position to observed ones, all within 50 d after orbit determination.

Fig. 1 shows that the angular distances are in general very small. The vast majority of the determined orbits produce distances smaller than 0.°6. Except for the first object, each object also shows some

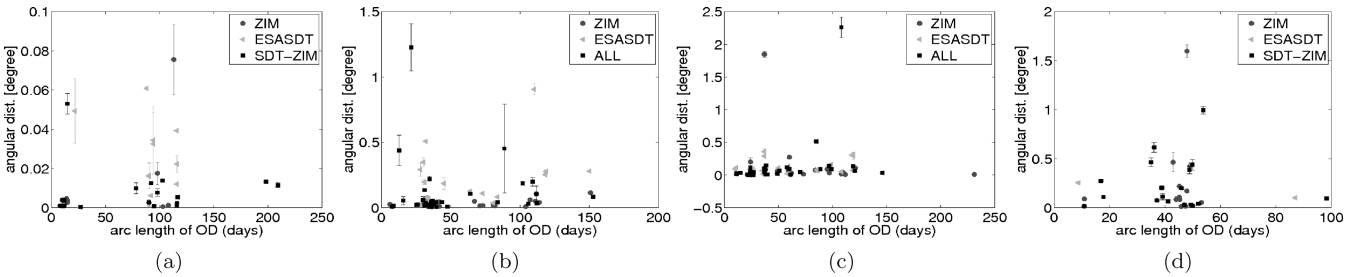

Figure 1. Angular distance as a function of the time interval between the first and the last observation of the fit interval of orbit determination for objects (a) E03174A, (b) E06321D, (c) E06327E and (d) E08241A.

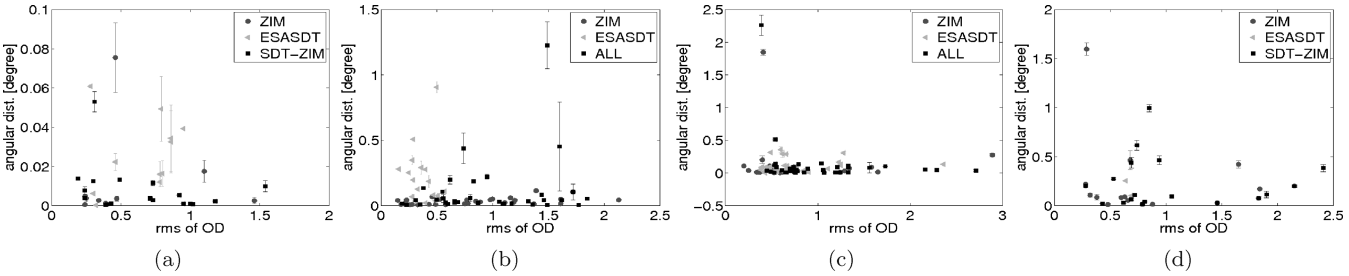

Figure 2. Root-mean-square of orbit determination as a function of the arclength of observations for objects (a) E03174A, (b) E06321D, (c) E06327E and (d) E08241A.

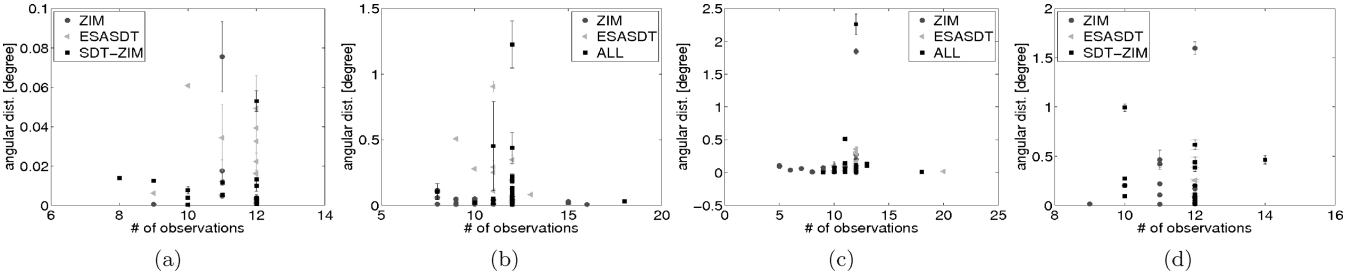

Figure 3. Angular distance as a function of the number of observations used for orbit determination for objects (a) E03174A, (b) E06321D, (c) E06327E and (d) E08241A.

outliers, with larger angular distances. These larger distances also tend to show larger standard deviations. The value of the angular distances seems to be, at least in this setup, quite independent of how large the difference between the first and the last observations of the fit interval is. Moreover, Fig. 1 also shows that there is no significant difference between using observations from only one observation site for orbit determination and using observations from two or more sites. It could not be shown that the latter approach is more advantageous for orbit determination, although multiple observation sites still have advantages in terms of availability and weather conditions, which results in a larger number of observations. Fig. 2 shows the root-mean-square of the orbit determinations that were used for the prediction as a function of the angular distance. No trend is visible; all orbits that were determined had a small root-mean-square of below 3 arcsec.

In Fig. 3, the angular distances are displayed as a function of the actual number of single observations that were involved in the orbit determination. It can be seen that no strong correlation is visible between the actual number of observations used and the value for the distances.

To find a measure for the true anomaly distribution, an anomaly distribution measure f_{ano} was defined: ideally, the n observations should be equally spaced with an angle of $2\pi/n$ between observations. The deviation from this ideal distribution is determined and normalized with the number of observations. The smaller f_{ano}, the better distributed are the observations in anomaly:

$$f_{\mathrm{ano}} = \frac{1}{n}\sqrt{\sum_{i=1}^{n-1}\left[\frac{2\pi}{n} - (a_{i+1} - a_i)\right]^2 + \left[\frac{2\pi}{n} - (a_1 + 2\pi - a_n)\right]^2}, \tag{2}$$

where n is the number of observations and a_i with $i = 1,\ldots,n$ are the anomalies of the single observations, in ascending anomaly order. The angular distances as a function of f_{ano} are displayed in Fig. 4. There is no clear correlation between the f_{ano} and the distances, as is expected for objects with small eccentricities. Object E06327E, with the highest eccentricity of $e = 0.06$, has the strongest correlation with f_{ano}.

The crucial factor, however, seems to be the time interval covered by the observations within the sets. In Fig. 5, the angular distance is displayed as a function of the time interval covered *within* the two sets used at the beginning and the end of the fit interval, without the time gap in between the two sets. A strong correlation is visible. Fig. 6 shows that there is no strong correlation between the

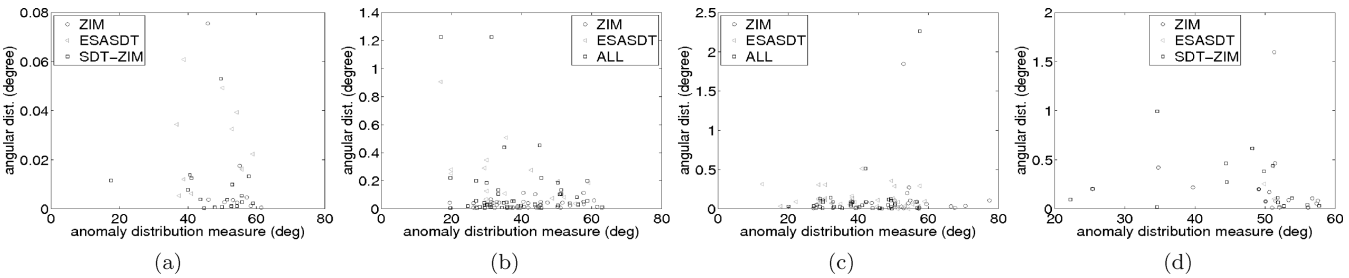

Figure 4. Angular distance as a function of the anomaly distribution factor for objects (a) E03174A, (b) E06321D, (c) E06327E and (d) E08241A.

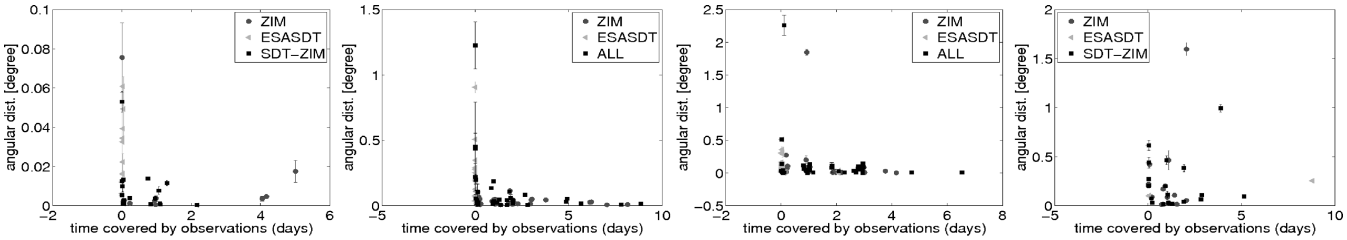

Figure 5. Angular distance as a function of the time interval covered by the observations used for orbit determination for objects (a) E03174A, (b) E06321D, (c) E06327E and (d) E08241A.

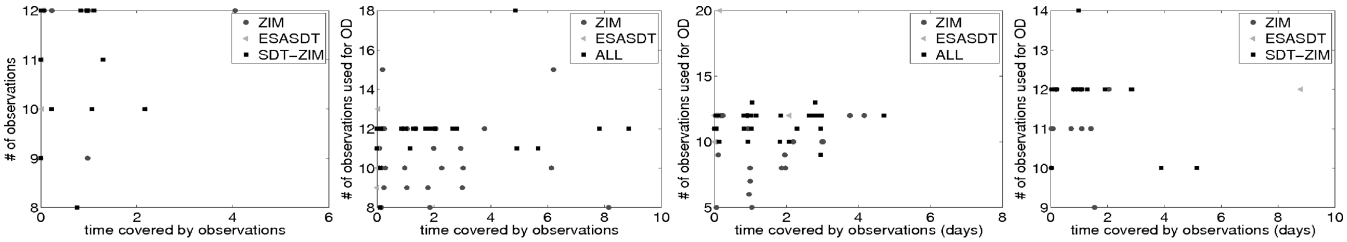

Figure 6. Time interval covered by the observations within the sets as a function of the number of observations used for orbit determination for objects (a) E03174A, (b) E06321D, (c) E06327E and (d) E08241A.

number of observations used and the time interval covered within the sets. For example, for the ESASDT observation strategy, primarily densely spaced observations are available.

An analysis of the data displayed in Fig. 6 showed that a coverage of at least 1.2 h for both sets together seems to be necessary to obtain an orbit that allows us to safely re-detect the investigated objects in more than 90 per cent of all cases with a field of view of one square degree; that is, to have an accuracy of below 0.5.

3 INVESTIGATION OF HAMR OBJECTS IN THE SPARSE DATA SETUP

The dynamical properties of HAMR objects were studied in the normalized sparse data setup established in the previous section. Orbits are determined with two observation sets only. The sets consist of four to eight observations each. The observations are required to span a time interval of at least 1.2 h within the sets and need to be well spread over the anomaly for the objects in orbits with a high eccentricity. The total fit interval for orbit determination ranges between 10 and 120 d. As shown in the previous section, the comparability of the orbits does not seem to be dependent on these ranges.

The orbits were first determined with observations from one observation site only, and then with observations from different sites in the setup mentioned above. The observations used in this investigation stem from the ESASDT, ZIMLAT and from several telescopes of the ISON network.

3.1 Selected objects

Five objects were selected for detailed investigation. All objects were discovered and first detected by the AIUB and are not listed in the USSTRATCOM catalogue. All objects are faint debris objects. They were tracked successfully over several years, and no manoeuvres were detected. A set of osculating orbital elements and average values for the apparent magnitudes are listed in Table 2. The two objects with the lowest AMR values, E08241A and E06321D, which were used in the investigation of the sparse data orbit determination, are used here again.

Table 2. Investigated high area-to-mass ratio objects. Internal name, epoch (MJD), eccentricity, inclination (°), semimajor axis (km), area-to-mass ratio ($m^2\ kg^{-1}$) and apparent magnitude (mag).

NAME	Epoch	*a*	*e*	*i*	AMR	Mag
E08241A	55213.0	41600	0.041	13.26	1.24	16.1
E06321D	55275.9	41400	0.035	7.00	2.29	15.3
E07194A	54877.0	40900	0.005	7.31	3.37	16.8
E07308B	54416.0	35600	0.264	7.63	8.83	15.8
E06293A	54951.0	40200	0.245	11.06	15.41	16.8

3.2 Evolution of orbital elements

The evolution of the orbital elements over time is inspected in a first step. Fig. 7 shows the development of the inclination and the errors in inclination of the five objects. The error bars are too small to be visible in the plot in most cases. The inclination values of the various orbits are closely aligned to each other and mark a consistent evolution. Only in the case of object E08241A in Fig. 7 can a wider spread in the inclination values be observed. The orbits determined with observations from the different observation sites produce almost identical results. For objects E07308B and E06293A, which have the highest AMR values, the inclination seems not to follow a steady increase over time, but some smaller periodic substructure seems to be superimposed. This may very well be the perturbations with a period of one nodal year, which are well known for objects with high AMR; see, for example, Liou & Weaver (2005), Schildknecht et al. (2005b).

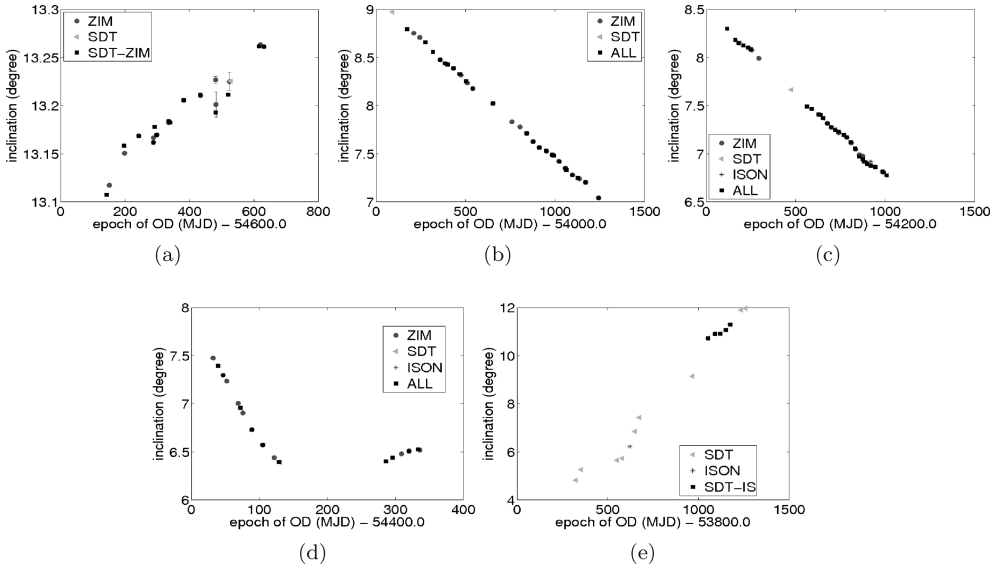

Figure 7. Inclination as a function of time for orbits of the objects (a) E08241A, (b) E06321D, (c) E07194A, (d) E07308B and (e) E06293A.

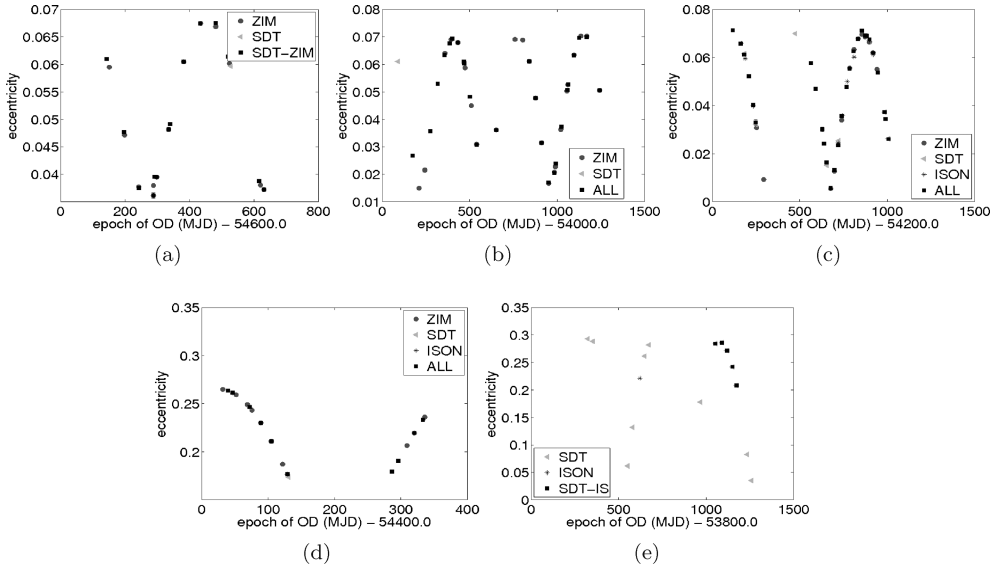

Figure 8. Eccentricity as a function of time for orbits of the objects (a) E08241A, (b) E06321D, (c) E07194A, (d) E07308B and (e) E06293A.

Fig. 8 shows the evolution of the eccentricity value and its errors estimated in the orbit determination for the various objects. Periodic variations can be observed for all objects. The various orbits with observations from one site only or from different sites result in the same eccentricities.

3.3 Evolution of AMR value

Fig. 9 shows the AMR values as a function of time for the objects listed in Table 2. In all cases, the values for the AMR do not show clear and obvious common trends; see Figs 7 and 8.

For object E08241A, the AMR values vary around a mean value of 1.4 $m^2\,kg^{-1}$ with no obvious trend or periodic signal; see Fig. 9(a).

For object E06321D (see Fig. 9b), the AMR value seems to vary periodically with a period of about 1 yr around a value of 2.5 $m^2\,kg^{-1}$, but values of 2.35 and 2.65 $m^2\,kg^{-1}$ also occur. Similar results were obtained by Musci et al. (2010), for the same object, in different orbit determination setups. The AMR value of object E07194A (see Fig. 9c) varies around 3.5 $m^2\,kg^{-1}$, but, in the orbits determined with combined observations from all the sites, so-called *outliers* of 4.5 and 2.3 $m^2\,kg^{-1}$ occur as well. These have, however, large error values.

Object E07308B (see Fig. 9d) seems to generally increase its AMR value over time from a value of 8.5 up to 9.0 $m^2\,kg^{-1}$. However, single orbits also show AMR values of, for example, 10 $m^2\,kg^{-1}$.

Fig. 9(e) shows that object E06293A, which is the object with the largest AMR value investigated here, has significant data gaps. A general trend of the AMR value in time, increasing from 15.5 to 16.5 $m^2\,kg^{-1}$, cannot be excluded. However, one orbit determined with ESASDT data also shows a value of 18.2 $m^2\,kg^{-1}$, with a small formal error.

No general correlation between the AMR value itself and the variations of the AMR value could be determined, and no general

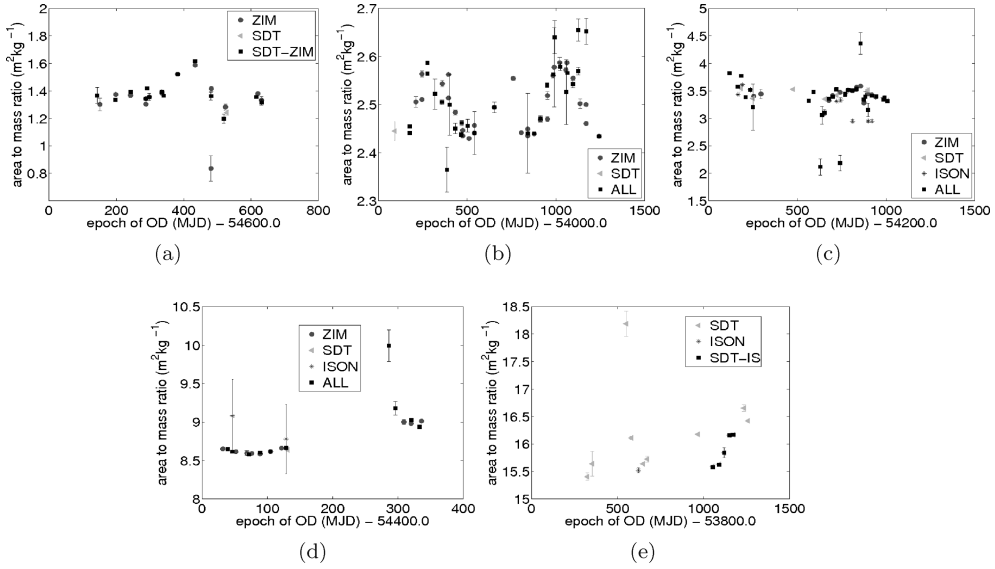

Figure 9. AMR as a function of time for orbits of the objects (a) E08241A, (b) E06321D, (c) E07194A, (d) E07308B and (e) E06293A.

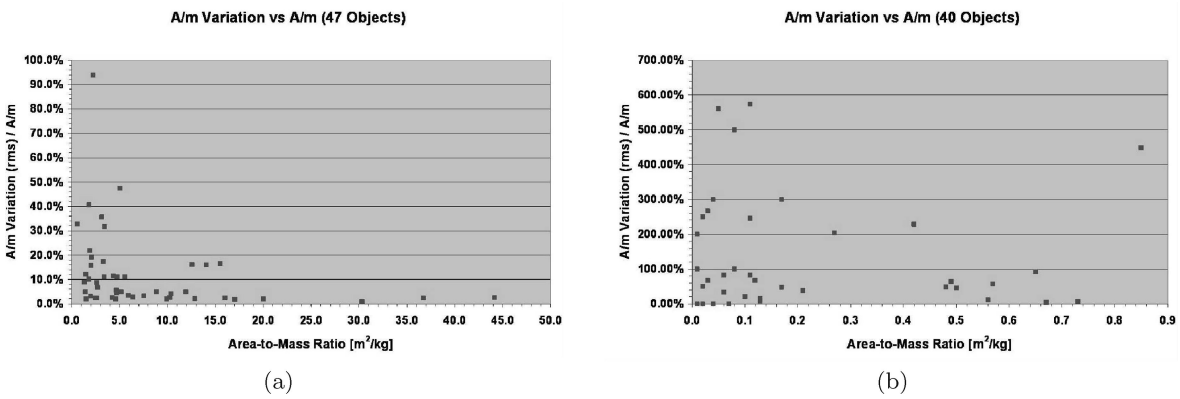

Figure 10. Relative variation of AMR value as a function of the absolute AMR value of (a) 47 HAMR and (b) LAMR objects.

trend is visible. A study of the variation of AMR values was conducted by T. Schildkecht (private communication). The variations of the AMR values of 47 HAMR objects were investigated and compared with the AMR variations of orbits of 40 low-AMR (LAMR) objects. No normalized or sparse data orbit determination setup was chosen. The AMR values in that analysis were determined with the standard orbit determination procedure for the AIUB, with fit arcs as long as possible for a successful (i.e. leading to a small rms error) orbit determination. The results are illustrated in Fig. 10. No general trend in the AMR variations could be determined for either HAMR or LAMR objects. The relative variations of the AMR values of the LAMR objects were larger than the AMR variations of the HAMR values. The AMR variations of the LAMR objects were of the order of several 100 per cent.

All orbits were predicted and compared with additional observations, which were not used for orbit determination, of the same object. The additional observations were all checked via orbit determination, to ensure that they belonged to the same object. Fig. 11 shows the angular distances between the predicted ephemeris and observations. The values are averaged over all distances 50 d after orbit determination, and their standard deviations serve as error bars.

Fig. 11(a) shows that for object E08241A, one orbit produces the largest distances of 1°. This orbit does not show up prominently in the orbital parameter plots (see Figs 8a and 7a) or in AMR value plots (see Fig. 9a). The orbit with ZIMLAT data, which produced the outlier AMR value of 0.82 $m^2\,kg^{-1}$, does not show up prominently in the distance plot (Fig. 11a).

The mean value of all angular distances of object E06321D are well below 0.2, but four orbits show large standard deviations in angular distance, as Fig. 11(b) shows. All of them were determined with combined observations from ZIMLAT, ESASDT and ISON. Their AMR values are 2.36, 2.50, 2.57 and 2.66 $m^2\,kg^{-1}$. The orbit with the AMR value of 2.36 $m^2\,kg^{-1}$ does show up also in a group of outlier AMR values, which do not seem to follow the periodic variation in the evolution of the AMR values. The other orbits, with large standard variations in angular distance, do not show up prominently (Fig. 9b). Those orbits with the largest standard variation in angular distance do not show the largest error in the AMR values either, as Fig. 13 shows.

Fig. 11(c) shows three angular distances with large standard deviations for object E07194A. The orbits were determined with observations from all sites. They have AMR values of 2.12, 2.21 and 4.46 $m^2\,kg^{-1}$. These are the smallest and largest AMR values in the

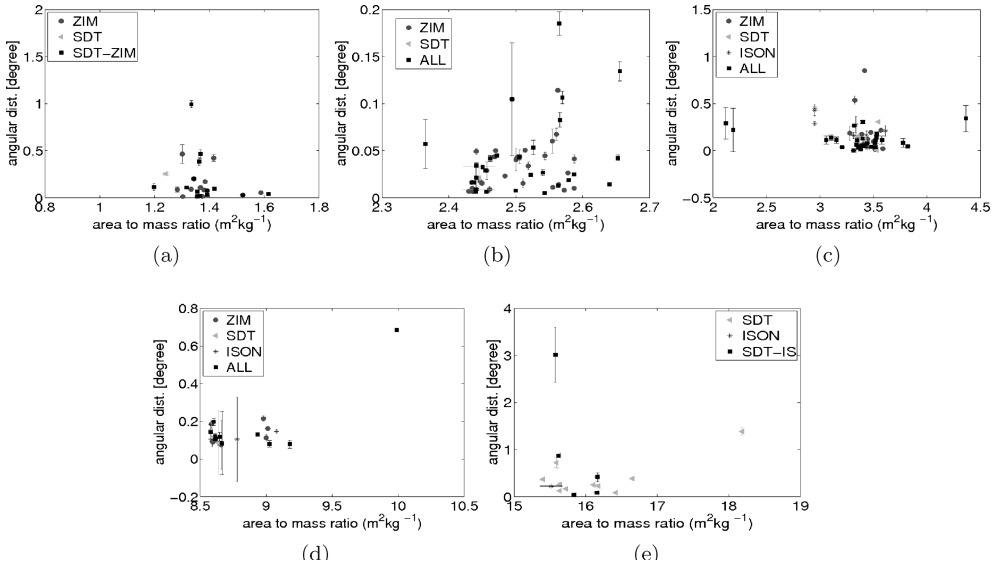

Figure 11. Angular distance of predicted orbits on the celestial sphere as a function of AMR for orbits of the objects (a) E08241A, (b) E06321D, (c) E07194A, (d) E07308B and (e) E06293A.

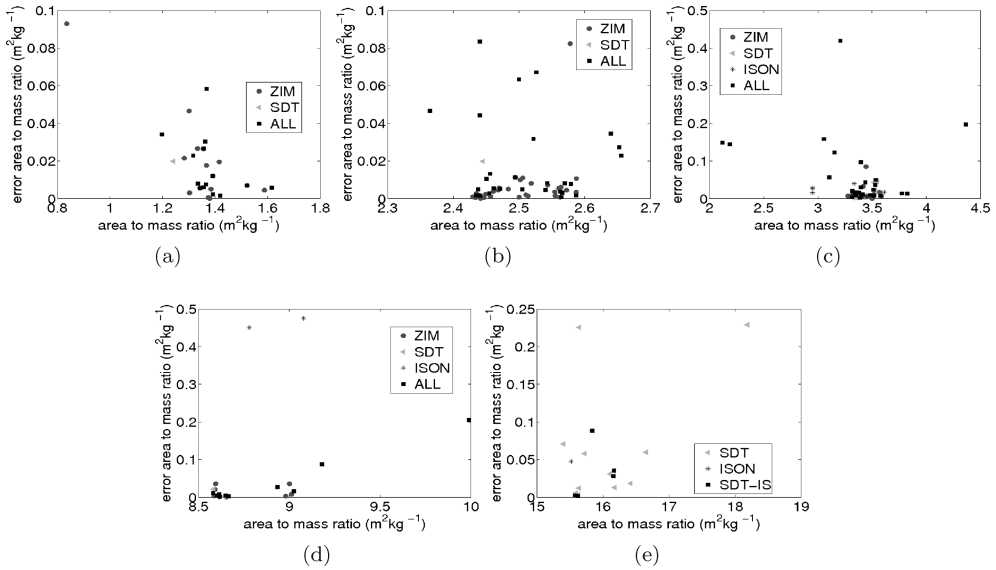

Figure 12. Error of the AMR value as a function of AMR as estimated in orbits of the objects (a) E08241A, (b) E06321D, (c) E07194A, (d) E07308B and (e) E06293A.

orbits determined for E07194A. These three values also show up as outliers in Fig. 9(c). For objects E07308B and E06293A, the angular distances with a large standard variation (see Figs 11d and e) do not show significant outlier AMR values in Figs 9(d) and (e). For object E07308B, the orbit with an AMR value of 10.15 $m^2\,kg^{-1}$ shows the largest mean value in the angular distance, of almost 0°.7, but has a small standard deviation at this distance (Fig. 11d). This value is significantly different from the other AMR values (see Fig. 9d).

The dependence of the AMR value on the error of the AMR, as found in the orbit determination, is investigated in the final step. No clear correlation could be determined between an AMR value and its rms value (Fig. 12).

Fig. 13 shows the angular distance on the celestial sphere as a function of the error of the AMR value. As expected, for none of the objects could a clear correlation between the error of the AMR value and the absolute value of the distances or the standard deviation of the distances be determined.

All investigated objects show variations in AMR value, but there is no common characteristic in these variations. It should be noted that the result may be affected by the relatively simple shadowing model that was used in orbit determination; as shown in Pardini & Anselmo (2008) and Valk & Lemaître (2008), shadowing effects have a significant influence on the long-term evolution of orbits of HAMR objects. An investigation of simulated orbits with numerical and semi-analytical methods, for example by Valk & Lemaître (2008) and Valk et al. (2008), also showed the existence of irregular chaotic orbits and the significant influence of secondary resonances on the orbits of HAMR objects. However, these simulations assumed a constant AMR value. Complex attitude motion, irregular shapes, and/or deformation of the actual objects could lead to a

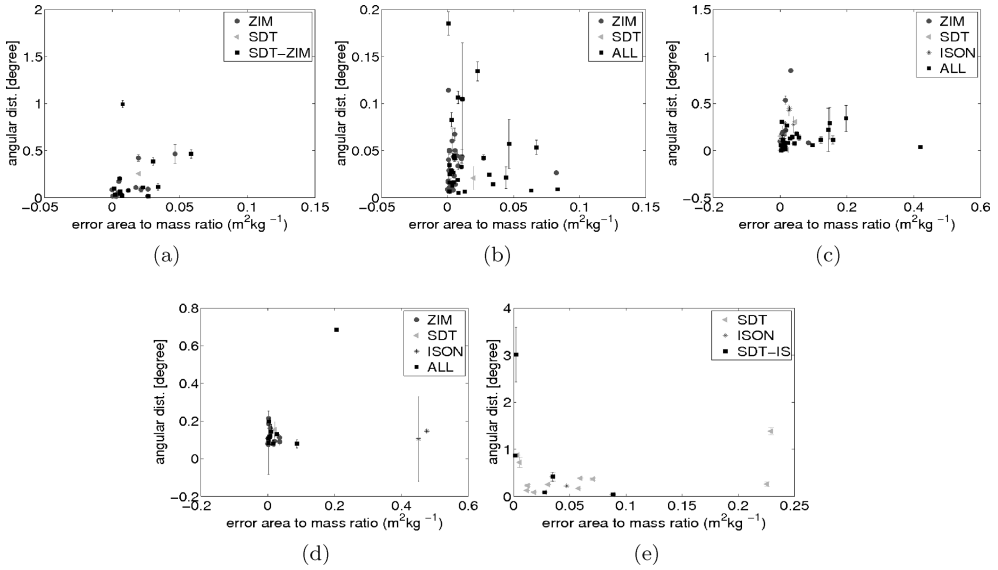

Figure 13. Absolute values and standard deviations of the angular distances as a function of the error of the AMR value as found in orbit determination of the objects (a) E08241A, (b) E06321D, (c) E07194A, (d) E07308B and (e) E06293A.

change in the AMR value itself over time, which may not be averaged out over the fit interval of orbit determination.

4 CONCLUSIONS

A sparse data setup was established to create comparable orbits over longer time intervals. Orbits with two data sets produce only small differences between the propagated ephemerides and further observations, as long as a time interval of 1.2 h is covered within the sets. Other factors, such as observations stemming from different sites or the time interval between the sets, are found to be negligible.

The orbits of HAMR objects were analysed in this setup. The AMR value, that is, the scaling factor of the direct radiation pressure parameter, varies over time. The order of magnitude of the variation of the AMR value is not correlated with the order of magnitude of its error.

The variation of the AMR is not averaged out in the fit interval of orbit determination. In the evolution of the AMR value over time, no common characteristic could be determined for different HAMR objects. Further work on the orbits of HAMR objects is needed, to improve the radiation pressure model, to determine possible attitude motion or deformations and to understand the resonance effects and the existence of chaotic regions.

ACKNOWLEDGMENTS

Special thanks go to ISON and the Keldysh Institute of Applied Mathematics, Moscow, for the supplementary observations.

This work was supported by the Swiss National Science Foundation through grants 200020-109527 and 200020-122070.

The observations from ESASDT were acquired under ESA/ESOC contracts 15836/01/D/HK and 17835/03/D/HK.

The authors thank the reviewer for useful comments.

REFERENCES

Beutler G., 2005, Methods of Celestial Mechanics, 2 Vols. Springer-Verlag, Heidelberg

Liou J.-C., Weaver J., 2005, in Danesy D., ed., Proc. 4th European Conf. on Space Debris. ESA, Noordwijk, p. 119

Musci R., Schildknecht T., Flohrer T., Beutler G., 2005, in Danesy D., ed., Proc. 4th European Conf. on Space Debris. ESA, Noordwijk, p. 601

Musci R., Schildknecht T., Ploner M., 2010, Acta Astron., 66, 693

Pardini C., Anselmo L., 2008, Trans. Japan Soc. Aero. Space Sci., 51, 22

Schildknecht T., Musci R., Ploner M., Flury W., Kuusela J., de Leon Cruz J., de Fatima Dominguez Palmero L., 2003, in Maui Economic Development Board, Inc., ed., Proc. 2003 AMOS Technical Conf. Curran Associates, Inc., p. 81

Schildknecht T., Musci R., Ploner M., Beutler G., Kuusela J., de Leon Cruz J., de Fatima Dominguez Palmero L., 2004, Adv. Space Res., 34, 901

Schildknecht T., Musci R., Flury W., Kuusela J., de Leon Cruz J., de Fatima Dominguez Palmero L.,, 2005a, in Danesy D., ed., Proc. 4th European Conf. on Space Debris. ESA, Noordwijk, p. 113

Schildknecht T., Musci R., Flury W., Kuusela J., de Leon Cruz J., de Fatima Dominguez Palmero L., 2005b, in Maui Economic Development Board, Inc., ed., Proc 2005 AMOS Technical Conf. Curran Associates, Inc., p. 134

Valk S., Lemaître A., 2008, Adv. Space Res., 42, 1429

Valk S., Delsate N., Lemaître A., Carletti T., 2008, Adv. Space Res., 43, 1509

Vallado D., McCain W., 2001, Fundmentals of Astrodynamics and Applications. Microcosm Press, El Segundo, CA

This paper has been typeset from a TEX/LATEX file prepared by the author.